

University of Nebraska - Lincoln

DigitalCommons@University of Nebraska - Lincoln

Faculty Publications, Department of Physics
and Astronomy

Research Papers in Physics and Astronomy

1-13-2023

In-plane ferroelectric tunnel junctions based on 2D α -In₂Se₃/ semiconductor heterostructures

Zifang Liu

Pengfei Hou

Lizhong Sun

Evgeny Y. Tsymbal

Jie Jiang

See next page for additional authors

Follow this and additional works at: <https://digitalcommons.unl.edu/physicsfacpub>



Part of the [Physics Commons](#)

This Article is brought to you for free and open access by the Research Papers in Physics and Astronomy at DigitalCommons@University of Nebraska - Lincoln. It has been accepted for inclusion in Faculty Publications, Department of Physics and Astronomy by an authorized administrator of DigitalCommons@University of Nebraska - Lincoln.

Authors

Zifang Liu, Pengfei Hou, Lihong Sun, Evgeny Y. Tsymbal, Jie Jiang, and Qiong Yang

ARTICLE OPEN

In-plane ferroelectric tunnel junctions based on 2D α - In_2Se_3 /semiconductor heterostructuresZifang Liu¹, Pengfei Hou¹, Lizhong Sun¹, Evgeny Y. Tsymbal^{1,2}, Jie Jiang¹✉ and Qiong Yang¹✉

Ferroelectric tunnel junctions (FTJs) have great potential for application in high-density non-volatile memories. Recently, α - In_2Se_3 was found to exhibit robust in-plane and out-of-plane ferroelectric polarizations at a monolayer thickness, which is ideal to serve as a ferroelectric component in miniaturized electronic devices. In this work, we design two-dimensional van der Waals heterostructures composed of an α - In_2Se_3 ferroelectric and a hexagonal IV–VI semiconductor and propose an in-plane FTJ based on these heterostructures. Our first-principles calculations show that the electronic band structure of the designed heterostructures can be switched between insulating and metallic states by ferroelectric polarization. We demonstrate that the in-plane FTJ exhibits two distinct transport regimes, tunneling and metallic, for OFF and ON states, respectively, leading to a giant tunneling electroresistance effect with the OFF/ON resistance ratio exceeding 1×10^4 . Our results provide a promising approach for the high-density ferroelectric memory based on the 2D ferroelectric/semiconductor heterostructures.

npj Computational Materials (2023)9:6; <https://doi.org/10.1038/s41524-022-00953-x>

INTRODUCTION

Ferroelectric materials are useful for information storage applications due to their spontaneous polarization which can be switched by an applied electric field. Driven by the demands of device miniaturization and non-volatility, a ferroelectric tunnel junction (FTJ) has been proposed and considered as one of the most promising memory types, as compared to the current commercial dynamic random-access memories^{1–5}. A typical FTJ is composed of two different electrodes separated by an ultrathin ferroelectric barrier layer^{6–9}. Due to the two electrodes and/or interfaces in a FTJs being asymmetric, the reversal of ferroelectric polarization leads to the variation of the height and/or width of the electron tunneling potential barrier, resulting in two distinct resistance states^{7,9–12}. This phenomenon is known as the tunneling electroresistance (TER) effect^{12–14}. So far, most FTJs utilized oxide perovskite ferroelectrics as barrier layers. Unfortunately, ferroelectricity of perovskite ferroelectric films often deteriorate at the nanoscale due to the well-known size effect¹⁵, making the miniaturization of the memory devices challenging.

In recent years, ferroelectricity was found in a few two-dimensional (2D) van der Waals (vdW) materials, such as CuInP_2S_6 ^{16,17}, WTe_2 ^{18,19}, and In_2Se_3 ^{20–22}. 2D vdW ferroelectrics are appealing due to their uniform atomic thickness, absence of dangling bonds, and the ability to be integrated with other vdW materials which allows useful functionalities. For example, in combination with conducting 2D materials, these 2D vdW ferroelectric materials can be used as ultrathin barriers in FTJs. Here we focus on α - In_2Se_3 which exhibits robust ferroelectricity even at a monolayer thickness and possesses intrinsically coupled out-of-plane (OOP) and in-plane (IP) ferroelectric polarizations^{20,23}. Its sizable polarization and a moderate ferroelectric switching energy barrier make α - In_2Se_3 attractive for memory devices, especially FTJs²⁴.

Since the discovery of ferroelectricity in 2D α - In_2Se_3 , plenty of experimental and theoretical works have been devoted to exploring its application in non-volatile memories^{25–34}. Wan

et al. demonstrated a ferroelectric field-effect transistor (FeFET) using ultrathin α - In_2Se_3 as a non-volatile ferroelectric gate and graphene as a conducting channel, which were separated by an insulating hexagonal boron nitride layer³⁵. Si et al. reported an asymmetric metal/ α - In_2Se_3 /Si crossbar ferroelectric semiconductor junction with an ON/OFF ratio $>10^4$ at room temperature³⁶. Also, several theoretic works have been published focusing on the band alignment of 2D α - In_2Se_3 heterostructures controlled by the OOP polarization of α - In_2Se_3 , which leads to about 1.1 eV potential difference between its two surfaces^{37–39}. Ferroelectric control of the band alignment is important for the design of FTJs and other types of memory devices. Wang et al. summarized different categories of the band alignment between ferroelectric α - In_2Se_3 and 2D semiconductors or metals³⁸.

A stronger polarization control of the band alignment in ferroelectric α - In_2Se_3 heterostructures and a simpler cell structure are still in focus for the memory application of 2D ferroelectrics. The recently proposed IP FTJs are especially interesting for the high-density information storage⁴⁰. Using this concept, Kang et al.^{41–43} explored IP 2D FTJs based on graphene/ α - In_2Se_3 vdW heterostructures, while Ding et al.⁴⁴ proposed an antiferroelectric-like behavior of bilayer In_2X_3 ($X = \text{S}, \text{Se}, \text{Te}$) to enhance the FTJ performance. Relevant to the above studies, Shen et al.⁴⁵ designed a 2D FTJ by p - and n -type doping at the two terminals of IP ferroelectric SnSe.

In this paper, we design a symmetric FTJs where both the ferroelectric barrier and the electrodes consist of layered vdW heterostructures. In these FTJs, the barrier layer represents an α - In_2Se_3 ferroelectric monolayer deposited on semiconductor monolayers, SnTe or PbSe, of hexagonal group IV–VI^{46,47}, while the electrodes are composed of a heavily electron-doped In_2Se_3 /SnTe bilayer, $(\text{In}_{0.5}\text{Sn}_{0.5})_2\text{Se}_3/(\text{Sn}_{0.5}\text{Sb}_{0.5})\text{Te}$. Using first-principles density functional theory (DFT) calculations, we demonstrate a robust ferroelectric polarization-controlled switching behavior between metallic and insulating states in the α - In_2Se_3 /SnTe (and α - In_2Se_3 /PbSe) ferroelectric heterostructures. By utilizing the

¹Hunan Provincial Key Laboratory of Thin Film Materials and Devices, School of Materials Science and Engineering, Xiangtan University, Xiangtan 411105 Hunan, China.

²Department of Physics and Astronomy, University of Nebraska, Lincoln, NE 68588, USA. ✉email: jiangjie@xtu.edu.cn; qyang@xtu.edu.cn

coupled IP and OOP ferroelectricity of α - In_2Se_3 and the ferroelectric-controlled band alignment of the designed vdW heterostructures, we propose a two-terminal IP 2D FTJ with a giant TER effect (OFF/ON resistance ratio $>1.2 \times 10^4$) and low ON state resistance. We infer the physical mechanism for the control of electron tunneling barriers and resulting transport properties for the ON and OFF states to be different and more effective as compared to those in the previous studies of IP FTJs. These results enrich the understanding of the ferroelectric band control in α - In_2Se_3 heterostructures and indicate a great potential for the 2D or ultrathin ferroelectrics for application in electronic devices.

RESULTS AND DISCUSSION

2D α - In_2Se_3 /semiconductor vdW heterostructures

We consider heterostructures of 2D ferroelectric α - In_2Se_3 interfaced with 2D semiconductors SnTe and PbSe. The three-fold rotational symmetry of all these 2D materials results in the same IP triangular cell shapes, as shown in Fig. 1a–c. The optimized IP lattice constants of monolayers α - In_2Se_3 , SnTe and PbSe (4.110, 4.172, and 4.096 Å, respectively) agree well with the existing results^{20,46–49}, leading to tolerable lattice mismatches of 1.4% ($\text{In}_2\text{Se}_3/\text{SnTe}$) and 0.05% ($\text{In}_2\text{Se}_3/\text{PbSe}$). Band gaps of monolayers α - In_2Se_3 , SnTe, and PbSe are calculated to be 0.78, 1.87, and 1.83 eV, respectively, which are in agreement with the existing results^{20,46–49} (see Supplementary Fig. 1 for their band structures).

Both Sn and Te terminations of SnTe at the interface with In_2Se_3 are considered in the heterostructures. The two terminations of SnTe in conjunction with two different OOP polarization directions of α - In_2Se_3 make four types of $\text{In}_2\text{Se}_3/\text{SnTe}$ heterostructures, as shown in Fig. 1d–g. The atomic configurations of the heterostructures are determined by translating the SnTe layer along the interface plane relative to the In_2Se_3 layer and fully relaxing the IP lattice parameters and atomic positions. Based on the structure optimization, it is found that each heterostructure has the global energy minimum with the top layer atoms of SnTe stacked directly under the top layer In atoms of In_2Se_3 . The IP lattice parameters for the four heterostructures shown in Fig. 1d–g are 4.113, 4.164, 4.080, and 4.086 Å, respectively. The distances between the top atomic plane of SnTe and the bottom Se atomic plane of In_2Se_3 for the four heterostructures are 2.822, 2.085, 2.976, and 2.815 Å, respectively.

The total energies of the four heterostructures (Fig. 1d–g) are calculated to be -1.971 , -2.127 , -1.947 , and -1.978 eV per unit cell, respectively (the total energy of separate In_2Se_3 and SnTe monolayers is set to be 0). It is seen that, the P_\uparrow state (where polarization of In_2Se_3 pointing away from SnTe) has 156 meV lower energy than the P_\downarrow state (where polarization of In_2Se_3 pointing into SnTe) for the Sn–Se interface heterostructure. This energy difference is much larger than the energy difference of 31 meV between the two polarization states for the Te–Se interface heterostructure. The larger energy difference between the two polarization states in the Sn–Se interface heterostructure relative to that in the Te–Se interface heterostructure originates from the interfacial Coulomb interaction. Due to the ionic bonding between the Sn cation and Se anion at the Sn–Se interface which reduces the electrostatic energy, this type of heterostructure is sensitive to the polarization direction of In_2Se_3 . When the polarization points away from the interface (P_\uparrow state), a negative polarization charge of the P_\uparrow state further reduces the electrostatic energy and leads to a smaller interlayer distance and an interfacial charge transfer (discussed below). On the contrary, due to the Coulomb repulsion between the Te and Se anions, the interfacial interaction at the Te–Se interface is much weaker. As a result, ferroelectric polarization reversal induced changes in the energy, interlayer distance, and interfacial charge transfer are insignificant. The obtained polarization states are stable and switchable as follows from the polarization switching study discussed in Supplementary Information (Supplementary Note 2 and Supplementary Fig. 2). Based on the same computational methods, $\text{In}_2\text{Se}_3/\text{PbSe}$ heterostructures exhibit similar energetics and structural properties (Supplementary Note 3 and Supplementary Fig. 3) to those of $\text{In}_2\text{Se}_3/\text{SnTe}$ heterostructures.

Next, we investigate the band alignment in the $\text{In}_2\text{Se}_3/\text{SnTe}$ heterostructures. Figure 2 displays the calculated band structures of the four heterostructures shown in Fig. 1d–g. For the P_\downarrow state of the Sn–Se interface heterostructure, the valence band maximum (VBM) and the conduction band minimum (CBM) are mainly contributed by SnTe and In_2Se_3 , respectively, resulting in an indirect band gap of 0.84 eV (Fig. 2a). If the polarization is reversed upward (P_\uparrow), the heterostructure becomes metallic (Fig. 2b) with the VBM (mainly contributed by SnTe) being 0.39 eV higher in energy than the CBM (mainly contributed by In_2Se_3). This transition to the metallic state is caused by the negative

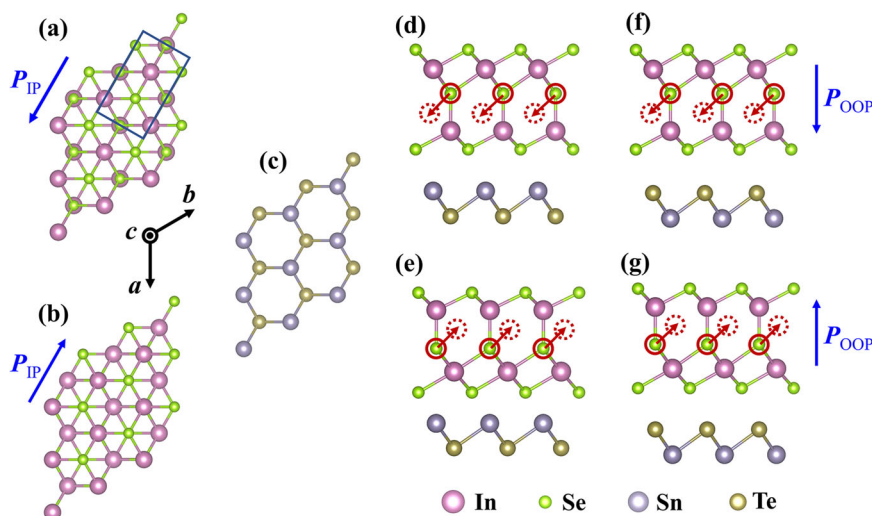


Fig. 1 Structural configurations of the heterostructures. **a, b** The top views of In_2Se_3 with downward (P_\downarrow) and upward (P_\uparrow) polarizations. **c** The top view of SnTe. **d–g** The side views of the four types of $\text{In}_2\text{Se}_3/\text{SnTe}$ heterostructures as seen against the a -axis in **a–c**. The seen monolayers and heterostructures are 3×3 expanded along the a - and b -axes relative to the unit cells for better visualization. Blue arrows represent the directions of the IP and OOP polarizations of In_2Se_3 . The red arrows in **d–g** indicate the moving directions of the central layer Se atoms if the In_2Se_3 are reversed from the current polarization states to the opposite polarization states.

ferroelectric polarization charge at the $\text{In}_2\text{Se}_3/\text{SnTe}$ interface lifting the electrostatic potential energy of SnTe up and resulting in an electron charge transferred from the SnTe valence band to the In_2Se_3 conduction band. This fact is evident from the atomic layer-resolved density of states (LDOS) and the charge transfer at the interface as illustrated in Supplementary Figs. 4 and 5. The predicted transition between insulating and metallic states for the Sn–Se interface heterostructure driven by polarization reversal from P_\downarrow to P_\uparrow is consistent with the type II to type III band alignment transition as defined in ref. ³⁸. The ferroelectric band control effect predicted in our study appears to be much more pronounced than those found in the similar 2D $\alpha\text{-In}_2\text{Se}_3$ /semiconductor heterostructures^{37,38,50}.

The Te–Se interface heterostructure behaves differently. In this case, the negative ionic charge of the Te atom at the interface bends the SnTe bands down thus pushing the In_2Se_3 up into the

band gap of SnTe. As a result, when polarization of In_2Se_3 is reversed, the change in the polarization charge at the interface is not sufficient to make the heterostructure metallic. We find that the P_\downarrow state exhibits an indirect band gap of 1.08 eV (Fig. 2c) with both VBM and CBM derived mainly from the In_2Se_3 layer, whereas the P_\uparrow state behaves an indirect band gap of 0.28 eV (Fig. 2d), where the VBM and CBM are contributed mainly by the SnTe and In_2Se_3 , respectively. This transition is consistent with the type I to type II band alignment transition as defined in ref. ³⁸.

The qualitative picture of the band alignment at the $\text{In}_2\text{Se}_3/\text{SnTe}$ interface, being dependent on ferroelectric polarization of In_2Se_3 and the interface termination, is described in Supplementary Note 6. The $\text{In}_2\text{Se}_3/\text{PbSe}$ heterostructures show similar electronic properties (Supplementary Note 7) to those of the $\text{In}_2\text{Se}_3/\text{SnTe}$ heterostructures.

In-plane ferroelectric tunnel junctions

The significant polarization-induced band tuning effect and the resulting transition between insulating and metallic states, makes the $\alpha\text{-In}_2\text{Se}_3$ ferroelectric heterostructures promising for application in memory and logic devices, such as FeFET and FTJs. In this work, we design an IP FTJ based on the Sn–Se terminated interface $\text{In}_2\text{Se}_3/\text{SnTe}$ heterostructure. The transport direction of the FTJ is set along the IP polarization direction of $\alpha\text{-In}_2\text{Se}_3$ (see Fig. 1a, b), which allows the simultaneous switching of OOP and IP polarizations through the application of an IP external electric field between the two electrodes. Figure 3 shows the atomic structures of the IP FTJs for the P_\downarrow and P_\uparrow states, respectively. The tunneling barrier in the FTJs consists of integer multiples (N) of the orthorhombic cells (denoted by the green rectangles in Figs. 1a and 3a) stacked along the transport direction. N is set to be ranging from 3 to 6. The lattice constant along the transport direction of each orthorhombic cell is 0.71 nm. Heavily electron-doped $\text{In}_2\text{Se}_3/\text{SnTe}$ heterostructures, namely $(\text{In}_{0.5}\text{Sn}_{0.5})_2\text{Se}_3/(\text{Sn}_{0.5}\text{Sb}_{0.5})\text{Te}$, are used as electrodes in the FTJs. Their electronic properties are obtained using the VCA⁵¹ by mixing 50% Sn on the In site and 50% Sb on the Sn site (see Supplementary Note 8 for the band structures of the electrodes).

Next, we explore the electron transport and the TER effect in $\text{In}_2\text{Se}_3/\text{SnTe}$ IP FTJs. Supplementary Fig. 9 shows the calculated transmission (T) as a function of electron energy (E) for the FTJs

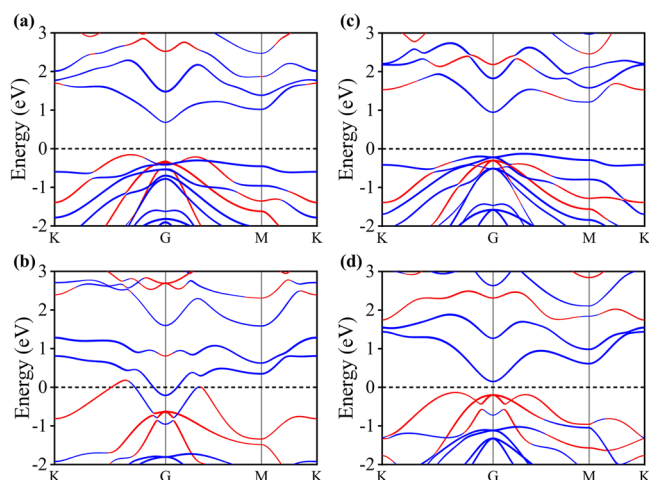


Fig. 2 Layer-projected band structures. The layer-projected band structures of the $\text{In}_2\text{Se}_3/\text{SnTe}$ heterostructures. **a** P_\downarrow state with Sn–Se interface, **b** P_\uparrow state with Sn–Se interface, **c** P_\downarrow state with Te–Se interface, **d** P_\uparrow state with Te–Se interface. The energy bands projected mainly on In_2Se_3 and SnTe layers are plotted in blue and red, respectively. The Fermi level is set to 0 eV.

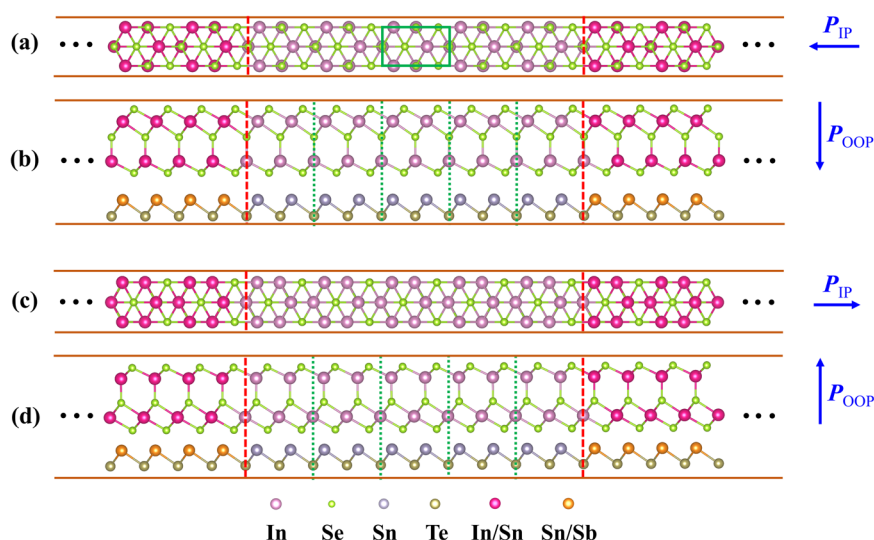


Fig. 3 Structural configurations of the IP FTJ. The atomic structures of $\text{In}_2\text{Se}_3/\text{SnTe}$ IP FTJs with $N=5$ for the **a, b** P_\downarrow and **c, d** P_\uparrow states. **a, c** are the top views. **b, d** are the side views seen against $a+b$ direction as defined in Fig. 1a–c. Red vertical dashed lines represent the boundaries between electrodes and the barrier layers. The deep green rectangle indicates one orthorhombic cell (two times of the hexagonal unit cell in volume) of the $\text{In}_2\text{Se}_3/\text{SnTe}$ barrier.

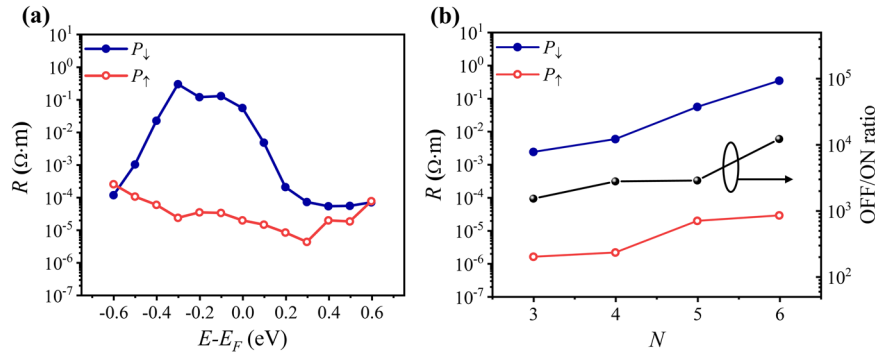


Fig. 4 The TER effect of FTJ. **a** The resistance (R) of the $\text{In}_2\text{Se}_3/\text{SnTe}$ IP FTJs with $N = 5$ for the P_\downarrow and P_\uparrow states as a function of electron energy E . **b** The resistance (R) and OFF/ON ratio of the FTJs at E_F while the orthorhombic cell number (N) of the barrier layer is varying from 3 to 6.

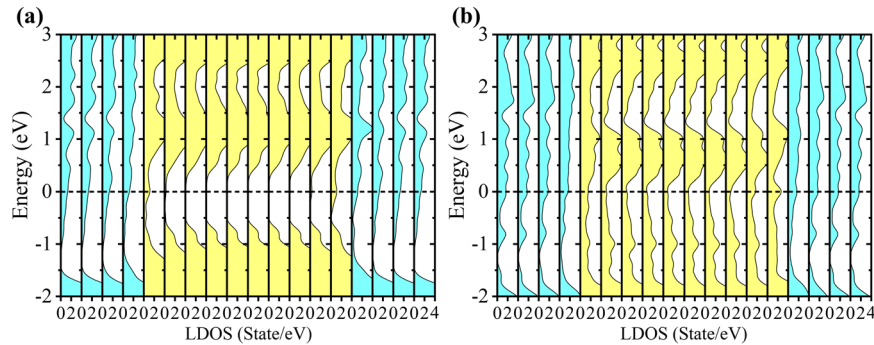


Fig. 5 The layer-resolved density of states of FTJ. Layer-resolved density of states (LDOS) projected on every half orthorhombic cell (including 2 In atoms, 3 Se atoms, 1 Sn atom, and 1 Te atom) of the IP FTJ along the transmission direction for **a** P_\downarrow states, **b** P_\uparrow states. LDOS of the $\text{In}_2\text{Se}_3/\text{SnTe}$ barrier layers and $(\text{In}_{0.5}\text{Sn}_{0.5})_2\text{Se}_3/(\text{Sn}_{0.5}\text{Sb}_{0.5})\text{Te}$ electrodes are plotted in yellow and blue, respectively.

with $N = 5$. It should be pointed out that the electronic structures of the electrodes for the P_\downarrow and P_\uparrow states are not the same due to the electrodes being constructed using the VCA from different atomic structure corresponding to P_\downarrow and P_\uparrow (Supplementary Fig. 8). To eliminate the effect of electrodes and obtain the genuine TER effect of the FTJ, the transmission of the pure electrodes is calculated and shown in Supplementary Fig. 10. Then, the resistance of the FTJ is calculated according to the formula: $R = d(h/e^2)[1/T_{\text{FTJ}} - 1/T_{\text{el}}]$ ⁵², where T_{FTJ} and T_{el} are the calculated transmissions of the FTJ (Supplementary Fig. 9) and electrodes (Supplementary Fig. 10), respectively, and d is the lattice constant perpendicular to the transport direction (0.41 nm). The calculated resistance (R) as a function of electron energy (E) of the FTJ with $N = 5$ for the P_\downarrow and P_\uparrow states is plotted in Fig. 4a. It is seen that, for the P_\downarrow state, the resistance increases significantly when the electron energy increases from $E_F - 0.6$ eV to $E_F - 0.3$ eV, and stays high until the energy increases up to E_F (E_F stands for the Fermi energy). Then the transmission gradually drops from E_F to $E_F + 0.2$ eV again as the energy keeps increasing. On the contrary, for the P_\uparrow state, the FTJ maintains a low resistance state under the considered electron energy range. The TER ratio (OFF/ON resistance ratio $R(P_\downarrow)/R(P_\uparrow)$) of the FTJ at $E = E_F$ is estimated to be 2.85×10^3 . For $E = E_F - 0.3$ eV, the OFF/ON ratio is found to be as large as 1.28×10^4 .

Then, the barrier width dependence of the TER effect is studied by calculating the resistance of FTJs at $E = E_F$ with the barrier layer width varying from 3 to 6 orthorhombic unit cells. It is seen from Fig. 4b that the resistance of the ON state (P_\uparrow state) stays low and is enhanced slowly when the barrier width increases. This is because, in the P_\uparrow state, the heterostructure is metallic, allowing the FTJ to behave like a conductor. On the contrary, for the OFF state (P_\downarrow state), the calculated resistance increases exponentially with increasing the barrier width, exhibiting a typical tunneling behavior. As a result, the OFF/ON resistance ratios are calculated

to be 1.51×10^3 , 2.76×10^3 , 2.85×10^3 , and 1.21×10^4 for the barrier layer width varying from 3 to 6 orthorhombic cells (Fig. 4b). We conclude, therefore, that the ferroelectric polarization induced TER effect in the designed $\text{In}_2\text{Se}_3/\text{SnTe}$ IP FTJ can be enhanced significantly by increasing the barrier width.

In order to understand the origin of this transport behavior, the electronic structure of the FTJ is analyzed. Figure 5 shows the calculated layer-resolved density of states (LDOS) along the width direction. Each panel in Fig. 5 displays the DOS projected on half an orthorhombic cell in the electrode and barrier regions for P_\downarrow (Fig. 5a) and P_\uparrow (Fig. 5b) states, respectively. As seen from Fig. 5a, the barrier layer exhibits a band gap from about -0.6 eV to 0.2 eV relative to E_F . This feature of the band structure well illustrates why the resistance of the P_\downarrow state increases and decreases at the energy of $E_F - 0.6$ eV and $E_F + 0.2$ eV, respectively, as shown in Fig. 4a (blue line). On the contrary, for the P_\uparrow state, as shown in Fig. 5b, there is no band gap across the barrier layer, leading to good conductivity under the entire considered energy range (see Fig. 4a, red line). The band structure-controlled insulating and conducting properties of the barrier layer for the P_\downarrow and P_\uparrow states also explain the barrier width dependence of the transport behavior shown in Fig. 4b.

To further clarify the transport mechanism of the designed IP FTJ, the partial charge densities in the real space are analyzed. Figure 6 visualizes the partial charge densities in the range of energies from $E_F - 0.1$ eV to E_F for P_\downarrow and P_\uparrow states, respectively. It is seen from Fig. 6a that, for the P_\downarrow state, the partial charge density at E_F only exists in the electrodes and a few atomic layers of the barrier near the interfaces, agreeing well with the LDOS of the FTJ at the Fermi energy in Fig. 5a. On the contrary, for the P_\uparrow state, as seen from Fig. 6b, there is abundant charge distributed within the barrier region, corresponding to the LDOS in Fig. 5b. From the spatial distribution, the partial charge density is mainly concentrated on the SnTe layer and the $\text{In}_2\text{Se}_3/\text{SnTe}$ interface in the

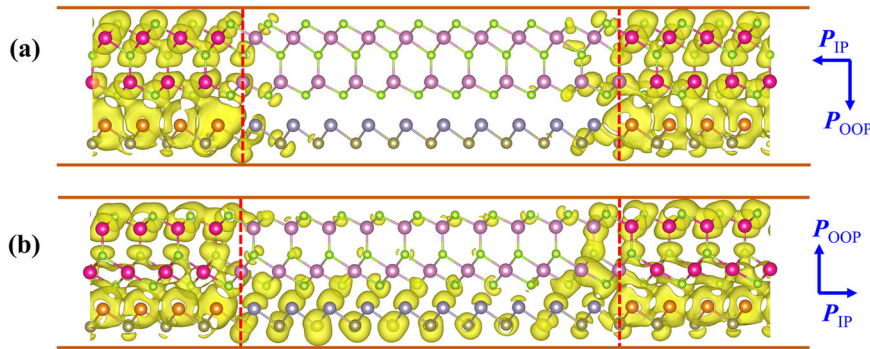


Fig. 6 The partial charge densities. The Partial charge densities for the designed FTJs in the energy range from $E_F - 0.1$ eV to E_F for **a** P_{\perp} and **b** P_{\parallel} state.

barrier region, which indicates that the electrons will transport along this channel as in a conductor under the external bias.

We would like to emphasize that the mechanism of TER considered in this work is different from those discussed previously, where asymmetry of an FTJ, i.e., different electrodes and/or different interfaces, was the necessary factor to obtain a large TER value. Here, a metal-insulator transition in the whole barrier layer is driven by the OOP polarization of In_2Se_3 and the FTJ asymmetry is not required. Contrary to the previous studies, the ferroelectric polarization that controls TER is pointing perpendicular to the transport direction, and the type of electrodes is not essential. Such design of the FTJ may be beneficial for applications because ON/OFF switching can be achieved in two ways: (1) by applying a bias voltage between the two electrodes to reverse the OOP polarization via reversal of the IP polarization as they are intrinsically coupled in ferroelectric In_2Se_3 , or (2) by applying a bias voltage to the top gate electrode to directly switch the OOP polarization as in a three-terminal FeFET.

In conclusion, we have designed vdW heterostructures with α - In_2Se_3 ferroelectric and hexagonal group IV–VI 2D semiconductor layers (SnTe and PbSe). Based on systematic first-principles studies, we demonstrated that these heterostructures exhibit a pronounced ferroelectric polarization control of the band alignment, which is promising for electronic device applications. We predicted that the $\text{In}_2\text{Se}_3/\text{SnTe}$ heterostructure with Sn–Se interface termination can be switched from the insulating state with a large band gap to the metallic state, when the OOP ferroelectric polarization of α - In_2Se_3 is reversed from pointing into to pointing away from 2D semiconductor layer. Driven by the polarization-controlled band alignment and the coupled IP and OOP ferroelectric polarizations in the designed $\text{In}_2\text{Se}_3/\text{SnTe}$ heterostructures, we proposed a functional two-terminal IP 2D FTJ. We predicted that the designed FTJ has two distinct electron transport mechanisms—tunneling and metallic for the OFF and ON states, respectively, resulting in a giant TER effect with the OFF/ON resistance ratio exceeding 1×10^4 . The predicted TER effect is significantly amplified by further increasing the barrier width of the FTJ. Our results are promising for the design of 2D ferroelectric heterostructures and FTJ-based non-volatile memories. We hope therefore that they will stimulate experimental efforts to explore such kind of FTJs in practice and demonstrate the predicted properties.

METHODS

Geometry optimization and electric structure calculations

DFT calculations using the projector augmented-wave as implemented in VASP code⁵³ are performed to optimize the monolayer 2D materials and heterostructures and study their electronic structures. The exchange–correlation effects are described by the Perdew–Burke–Ernzerhof generalized gradient approximation⁵⁴.

The plane-wave cutoff energy is set to be 500 eV. The $12 \times 12 \times 1$ and $21 \times 21 \times 1$ Monkhorst–Pack k-point meshes for the irreducible Brillouin zone sampling are used in the geometric optimization and subsequent self-consistent calculation of the heterostructures. Vacuum layers thicker than 15 Å are set along the normal direction to avoid the interaction between the top and bottom surfaces. The vdW interactions are treated using the DFT–D3 corrections⁵⁵. The IP lattice parameters and atomic positions are fully relaxed until the Hellmann–Feynman force on each atom is less than 0.005 eV/Å.

Electron transport calculations

The IP FTJs are constructed along the IP polarization direction based on the relaxed $\text{In}_2\text{Se}_3/\text{SnTe}$ heterostructures. The barrier region consists of several unit cells of $\text{In}_2\text{Se}_3/\text{SnTe}$, and the electrodes are treated using the virtual crystal approximation⁵¹ where the In site of In_2Se_3 is occupied by $\text{In}_{0.5}\text{Sn}_{0.5}$ and the Sn site of SnTe is occupied by $\text{Sn}_{0.5}\text{Sb}_{0.5}$ thus simulating the *n*-type doping. The electron transmissions across the FTJ are calculated within the general scattering formalism⁵⁶ as implemented in Quantum ESPRESSO⁵⁷. The designed IP FTJs and the $(\text{In}_{0.5}\text{Sn}_{0.5})_2\text{Se}_3/(\text{Sn}_{0.5}\text{Sb}_{0.5})\text{Te}$ heterostructures are used as the scattering regions and semi-infinite leads, respectively. A uniform 50×10 k_{\parallel} -mesh is used to sample the two-dimension Brillouin zone in transmission calculation.

DATA AVAILABILITY

The data that support the findings of the work is in the manuscript's main text and Supplementary Information. Additional data are available from the corresponding author upon reasonable request.

CODE AVAILABILITY

The central codes used in this paper are VASP and Quantum ESPRESSO.

Received: 13 May 2022; Accepted: 10 December 2022;

Published online: 13 January 2023

REFERENCES

- Esaki, A. L., Laibowitz, R. & Stiles, P. Polar switch. *IBM Tech. Discl. Bull.* **13**, 114 (1971).
- Tsymbal, E. Y. & Kohlstedt, H. Tunneling across a ferroelectric. *Science* **313**, 181–183 (2006).
- Kohlstedt, H., Pertsev, N. A., Contreras, J. R. & Waser, R. Theoretical current-voltage characteristics of ferroelectric tunnel junctions. *Phys. Rev. B* **72**, 125341 (2005).
- Kim, D. J. et al. Ferroelectric tunnel memristor. *Nano Lett.* **12**, 5697–5702 (2012).
- Garcia, V. & Bibes, M. Ferroelectric tunnel junctions for information storage and processing. *Nat. Commun.* **5**, 4289 (2014).
- Xi, Z. et al. Giant tunnelling electroresistance in metal/ferroelectric/semiconductor tunnel junctions by engineering the Schottky barrier. *Nat. Commun.* **8**, 15217 (2017).

7. Wen, Z., Li, C., Wu, D., Li, A. & Ming, N. Ferroelectric-field-effect-enhanced electroresistance in metal/ferroelectric/semiconductor tunnel junctions. *Nat. Mater.* **12**, 617–621 (2013).
8. Pantel, D. et al. Tunnel electroresistance in junctions with ultrathin ferroelectric $\text{Pb}(\text{Zr}_{0.2}\text{Ti}_{0.8})\text{O}_3$ barriers. *Appl. Phys. Lett.* **100**, 232902 (2012).
9. Velev, J. P., Burton, J. D., Zhuravlev, M. Y. & Tsybmal, E. Y. Predictive modelling of ferroelectric tunnel junctions. *NPJ Comput. Mater.* **2**, 16009 (2016).
10. Liu, X., Burton, J. D. & Tsybmal, E. Y. Enhanced tunneling electroresistance in ferroelectric tunnel junctions due to the reversible metallization of the barrier. *Phys. Rev. Lett.* **116**, 197602 (2016).
11. Wu, Q. et al. Giant tunneling electroresistance induced by ferroelectrically switchable two-dimensional electron gas at nonpolar $\text{BaTiO}_3/\text{SrTiO}_3$ interface. *Phys. Rev. B* **94**, 155420 (2016).
12. Yang, Q. et al. Ferroelectric tunnel junctions enhanced by a polar oxide barrier layer. *Nano Lett.* **19**, 7385–7393 (2019).
13. Zhuravlev, M. Y., Sabirianov, R. F., Jaswal, S. S. & Tsybmal, E. Y. Giant electroresistance in ferroelectric tunnel junctions. *Phys. Rev. Lett.* **94**, 246802 (2005).
14. Zhuravlev, M. Y., Maekawa, S. & Tsybmal, E. Y. Effect of spin-dependent screening on tunneling electroresistance and tunneling magnetoresistance in multiferroic tunnel junctions. *Phys. Rev. B* **81**, 104419 (2010).
15. Junquera, J. & Ghosez, P. Critical thickness for ferroelectricity in perovskite ultrathin films. *Nature* **422**, 506–509 (2003).
16. Liu, F. et al. Room-temperature ferroelectricity in CuInP_2S_6 ultrathin flakes. *Nat. Commun.* **7**, 12357 (2016).
17. Brehm, J. A. et al. Tunable quadruple-well ferroelectric van der Waals crystals. *Nat. Mater.* **19**, 43–48 (2020).
18. Sharma, P. et al. A room-temperature ferroelectric semimetal. *Sci. Adv.* **5**, eaax0580 (2019).
19. Fei, Z. et al. Ferroelectric switching of a two-dimensional metal. *Nature* **560**, 336–339 (2018).
20. Ding, W. et al. Prediction of intrinsic two-dimensional ferroelectrics in In_2Se_3 and other $\text{III}_2\text{-VI}_3$ van der Waals materials. *Nat. Commun.* **8**, 14956 (2017).
21. Xiao, J. et al. Intrinsic two-dimensional ferroelectricity with dipole locking. *Phys. Rev. Lett.* **120**, 227601 (2018).
22. Zheng, C. et al. Room temperature in-plane ferroelectricity in van der Waals In_2Se_3 . *Sci. Adv.* **4**, eaar7720 (2018).
23. Cui, C. et al. Intercorrelated in-plane and out-of-plane ferroelectricity in ultrathin two-dimensional layered semiconductor In_2Se_3 . *Nano Lett.* **18**, 1253–1258 (2018).
24. Su, Y. et al. Van der Waals multiferroic tunnel junctions. *Nano Lett.* **21**, 175–181 (2021).
25. Xue, F. et al. Gate-tunable and multidirection-switchable memristive phenomena in a van der Waals ferroelectric. *Adv. Mater.* **31**, 1901300 (2019).
26. Xie, S. et al. Ferroelectric semiconductor junctions based on graphene/ In_2Se_3 /graphene van der Waals heterostructures. *2D Mater.* **8**, 045020 (2021).
27. Wang, S. et al. Two-dimensional ferroelectric channel transistors integrating ultrafast memory and neural computing. *Nat. Commun.* **12**, 53 (2021).
28. Su, H., Hu, T., Wu, F. & Kan, E. Controllable vdW contacts between the ferroelectric In_2Se_3 monolayer and two-dimensional metals. *J. Phys. Chem. C* **125**, 10738–10746 (2021).
29. Mukherjee, S. & Koren, E. Indium selenide (In_2Se_3)—an emerging van-der-Waals material for photodetection and non-volatile memory applications. *Isr. J. Chem.* **62**, e202100112 (2022).
30. Hu, H. & Ouyang, G. First-principles calculations of interface engineering for 2D $\alpha\text{-In}_2\text{Se}_3$ -based van der Waals multiferroic heterojunctions. *Appl. Surf. Sci.* **545**, 149024 (2021).
31. Cheng, H.-X., Zhou, J., Wang, C., Ji, W. & Zhang, Y.-N. Nonvolatile electric field control of magnetism in bilayer CrI_3 on monolayer In_2Se_3 . *Phys. Rev. B* **104**, 064443 (2021).
32. Wan, S. et al. Room-temperature ferroelectricity and a switchable diode effect in two-dimensional $\alpha\text{-In}_2\text{Se}_3$ thin layers. *Nanoscale* **10**, 14885–14892 (2018).
33. Poh, S. M. et al. Molecular-beam epitaxy of two-dimensional In_2Se_3 and its giant electroresistance switching in ferroresistive memory junction. *Nano Lett.* **18**, 6340–6346 (2018).
34. Li, Y. et al. Orthogonal electric control of the out-of-plane field-effect in 2D ferroelectric $\alpha\text{-In}_2\text{Se}_3$. *Adv. Electron. Mater.* **6**, 2000061 (2020).
35. Wan, S. et al. Nonvolatile ferroelectric memory effect in ultrathin $\alpha\text{-In}_2\text{Se}_3$. *Adv. Funct. Mater.* **29**, 1808606 (2019).
36. Si, M. et al. Asymmetric metal/ $\alpha\text{-In}_2\text{Se}_3$ /Si crossbar ferroelectric semiconductor junction. *ACS Nano* **15**, 5689–5695 (2021).
37. Zhou, B. et al. Ferroelectric and dipole control of band alignment in the two dimensional $\text{InTe}/\text{In}_2\text{Se}_3$ heterostructure. *J. Phys. Condens. Matter* **32**, 055703 (2019).
38. Wang, Z. & Zhu, W. Tunable band alignments in 2D ferroelectric $\alpha\text{-In}_2\text{Se}_3$ based van der Waals heterostructures. *ACS Appl. Electron. Mater.* **3**, 5114–5123 (2021).
39. Ayadi, T. et al. An ab initio study of the ferroelectric In_2Se_3 /graphene heterostructure. *Phys. E Low. Dimens. Syst. Nanostruct.* **114**, 113582 (2019).
40. Shen, H., Liu, J., Chang, K. & Fu, L. In-plane ferroelectric tunnel junction. *Phys. Rev. Appl.* **11**, 024048 (2019).
41. Kang, L. et al. Domain-wall induced giant tunneling electroresistance effect in two-dimensional graphene/ In_2Se_3 ferroelectric tunnel junctions. *Phys. E Low. Dimens. Syst. Nanostruct.* **133**, 114783 (2021).
42. Kang, L. et al. Giant tunnel electroresistance in ferroelectric tunnel junctions with metal contacts to two-dimensional ferroelectric materials. *Phys. Rev. B* **103**, 125414 (2021).
43. Kang, L. et al. Giant tunneling electroresistance in two-dimensional ferroelectric tunnel junctions with out-of-plane ferroelectric polarization. *Phys. Rev. B* **101**, 014105 (2020).
44. Ding, J., Shao, D.-F., Li, M., Wen, L.-W. & Tsybmal, E. Y. Two-dimensional anti-ferroelectric tunnel junction. *Phys. Rev. Lett.* **126**, 057601 (2021).
45. Shen, X.-W., Fang, Y.-W., Tian, B.-B. & Duan, C.-G. Two-dimensional ferroelectric tunnel junction: the case of monolayer $\text{In}_2\text{SnSe}/\text{SnSe}/\text{Sb}_2\text{SnSe}$ homostructure. *ACS Appl. Electron. Mater.* **1**, 1133–1140 (2019).
46. Kamal, C., Chakrabarti, A. & Ezawa, M. Direct band gaps in group IV-VI monolayer materials: binary counterparts of phosphorene. *Phys. Rev. B* **93**, 125428 (2016).
47. Tian, X.-Q. et al. Hexagonal layered group IV-VI semiconductors and derivatives: fresh blood of the 2D family. *Nanoscale* **12**, 13450–13459 (2020).
48. Fatahi, N. et al. 2D Hexagonal SnTe monolayer: a quasi direct band gap semiconductor with strain sensitive electronic and optical properties. *Eur. Phys. J. B* **93**, 32 (2020).
49. Allaoui, I., Benyoussef, A. & El Kenz, A. Two-dimensional SnTe/Sb van der Waals heterostructure for photovoltaic application. *Solid State Sci.* **121**, 106736 (2021).
50. Ayadi, T. et al. An ab initio study of the electronic properties of the ferroelectric heterostructure $\text{In}_2\text{Se}_3/\text{Bi}_2\text{Se}_3$. *Appl. Surf. Sci.* **538**, 148066 (2021).
51. Fang, Z., Solovyev, I. V. & Terakura, K. Phase diagram of tetragonal manganites. *Phys. Rev. Lett.* **84**, 3169–3172 (2000).
52. Xia, K. et al. Interface resistance of disordered magnetic multilayers. *Phys. Rev. B* **63**, 064407 (2001).
53. Kresse, G. & Joubert, D. From ultrasoft pseudopotentials to the projector augmented-wave method. *Phys. Rev. B* **59**, 1758–1775 (1999).
54. Perdew, J. P., Burke, K. & Ernzerhof, M. Generalized gradient approximation made simple. *Phys. Rev. Lett.* **77**, 3865–3868 (1996).
55. Grimme, S., Antony, J., Ehrlich, S. & Krieg, H. A consistent and accurate ab initio parametrization of density functional dispersion correction (DFT-D) for the 94 elements H-Pu. *J. Chem. Phys.* **132**, 154104 (2010).
56. Smogunov, A., Dal Corso, A. & Tosatti, E. Ballistic conductance of magnetic Co and Ni nanowires with ultrasoft pseudopotentials. *Phys. Rev. B* **70**, 045417 (2004).
57. Giannozzi, P. et al. QUANTUM ESPRESSO: a modular and open-source software project for quantum simulations of materials. *J. Phys. Condens. Matter* **21**, 395502 (2009).

ACKNOWLEDGEMENTS

The authors thank Dr. Lingling Tao for helpful discussions. This work was supported by the National Natural Science Foundation of China (Grant Nos. 12072307 and 12175191), the Outstanding Youth Science Foundation of Hunan Province, China (Grant No. 2021JJ20041) and the Research Foundation of Education Bureau of Hunan Province, China (Grant No. 21A0114). The atomic structures were plotted using VESTA software.

AUTHOR CONTRIBUTIONS

Q.Y. and J.J. designed the idea of the research. Z.L. performed the first-principles calculations and wrote the manuscript. All the authors contributed to the general discussion, review and editing. Q.Y. supervised the research.

COMPETING INTERESTS

The authors declare no competing interests.

ADDITIONAL INFORMATION

Supplementary information The online version contains supplementary material available at <https://doi.org/10.1038/s41524-022-00953-x>.

Correspondence and requests for materials should be addressed to Jie Jiang or Qiong Yang.

Reprints and permission information is available at <http://www.nature.com/reprints>

Publisher's note Springer Nature remains neutral with regard to jurisdictional claims in published maps and institutional affiliations.



Open Access This article is licensed under a Creative Commons Attribution 4.0 International License, which permits use, sharing, adaptation, distribution and reproduction in any medium or format, as long as you give appropriate credit to the original author(s) and the source, provide a link to the Creative Commons license, and indicate if changes were made. The images or other third party material in this article are included in the article's Creative Commons license, unless indicated otherwise in a credit line to the material. If material is not included in the article's Creative Commons license and your intended use is not permitted by statutory regulation or exceeds the permitted use, you will need to obtain permission directly from the copyright holder. To view a copy of this license, visit <http://creativecommons.org/licenses/by/4.0/>.

© The Author(s) 2023